ADVANCED OPTICAL MATERIALS
www.advopticalmat.de

Nanoscale Photoluminescence Manipulation in Monolithic Porous Silicon Oxide Microcavity Coated with Rhodamine-Labeled Polyelectrolyte via Electrostatic Nanoassembling

Zhi Chen, Valentina Robbiano, Giuseppe M. Paternò, Giuseppe Carnicella, Aline Debrassi, Antonino A. La Mattina, Stefano Mariani, Alessandro Minotto, Gabriella Egri, Lars Dähne, Franco Cacialli, and Giuseppe Barillaro**

Porous silicon (PSi) is a promising material for future integrated nanophotonics when coupled with guest emitters, still facing challenges in terms of homogenous distribution and nanometric thickness of the emitter coating within the silicon nanostructure. Herein, it is shown that the nanopore surface of a porous silicon oxide ($PSiO_2$) microcavity (MC) can be conformally coated with a uniform nm-thick layer of a cationic light-emitting polyelectrolyte, e.g., poly(allylamine hydrochloride) labeled with Rhodamine B (PAH-RhoB), leveraging the self-tuned electrostatic interaction of the positively-charged PAH-RhoB polymer and negatively-charged $PSiO_2$ surface. It is found that the emission of PAH-RhoB in the $PSiO_2$ MC is enhanced (≈2.5×) and narrowed (≈30×) at the resonant wavelength, compared with that of PAH-RhoB in a non-resonant $PSiO_2$ reference structure. The time-resolved photoluminescence analysis highlights a shortening (≈20%) of the PAH-RhoB emission lifetime in the $PSiO_2$ MC at the resonance versus off-resonance wavelengths, and with respect to the reference structure, thereby proving a significant variation of the radiative decay rate. Remarkably, an experimental Purcell factor $F_p = 2.82$ is achieved. This is further confirmed by the enhancement of the photoluminescence quantum yield of the PAH-RhoB in the $PSiO_2$ MC with respect to the reference structure. Application of the electrostatic nanoassembling approach to other emitting dyes, nanomaterials, and nanophotonic systems is envisaged.

1. Introduction

Porous silicon (PSi) is recognized as a powerful supplement in future silicon-based integrated nanophotonics.[1–7] An ideal strategy is simultaneously leveraging the photoluminescence (PL) emission[1,2] and flexible fabrication of photonic nano-/mesostructures in PSi[4,7] for emerging integrated nanophotonic devices. However, such a strategy has been hampered by the low quantum efficiency and relatively poor stability of PL in PSi nanostructures.[1,2,8] An alternative strategy is leveraging the intrinsic material porosity to couple high-efficiency light-emitting guest nanomaterials with PSi-based nanophotonic devices to gain novel optical features and improve optical performance.

Thanks to its versatile, robust, and high-yield modulation of refractive index and unique nano/mesoporous structure,[9,10] PSi permits facile fabrication of photonic devices, in particular of microcavities (MCs), and easy introduction of guest emitters. Recently, oxidized porous silicon ($PSiO_2$) has been employed for the fabrication of a number of advanced photonic devices, such as 3D poly(dimethylsiloxane) (PDMS) lenses incorporating 1D photonic crystal components,[11] and 2D/3D gradient refractive index optical elements.[4,12] Further, infiltration of PSi with a number of nanomaterials has been carried out to take advantage of the peculiar properties of luminescent guest materials when confined within silicon-based photonic structures with characteristic length down to the meso-to-nanoscale.[11,13,14]

Z. Chen, V. Robbiano, A. A. La Mattina, S. Mariani, G. Barillaro
Dipartimento di Ingegneria dell'Informazione
Università di Pisa
Via G. Caruso 16, Pisa 56122, Italy
E-mail: giuseppe.barillaro@unipi.it

The ORCID identification number(s) for the author(s) of this article can be found under https://doi.org/10.1002/adom.202100036.

DOI: 10.1002/adom.202100036

G. M. Paternò
Center for Nano Science and Technology@PoliMi
Istituto Italiano di Tecnologia
Via Giovanni Pascoli, 70/3, Milano 20133, Italy

G. Carnicella, A. Minotto, F. Cacialli
Department of Physics and Astronomy and London Centre for Nanotechnology
University College London
Gower Street, London WC1E 6BT, UK
E-mail: f.cacialli@ucl.ac.uk

A. Debrassi, G. Egri, L. Dähne
Surflay Nanotec GmbH
Max-Planck-Straße 3, 12489 Berlin, Germany

Several research groups have reported on the use of monolithic and hybrid PSi-based MCs for controlling the spontaneous emission (SE) of emitters, by pore impregnation with dyes[15] or functionalization with rare-earth ions,[16,17] direct or indirect thin-film deposition of quantum dots (QDs),[7,18] and direct one-step infiltration of conjugated polymers[19,20] and QDs.[21] Remarkably, we have recently achieved low-threshold blue lasing from poly(9,9-di-n-octylfluorenyl-2,7-diyl) (PFO) confined within $PSiO_2$ MCs.[22] The direct/indirect thin-film deposition approach relies on a complex multi-step fabrication of hybrid PSi MCs exploiting QD thin films deposited between the two PSi-based distributed Bragg reflectors (DBRs) as the cavity layer. This approach fails to provide precise control over thickness and uniformity of the cavity layer embedding the guest emitter, which eventually results in a sub-optimal coupling of the emitters within the cavity. On the other hand, impregnation, functionalization, and direct one-step infiltration strategies of monolithic PSi MCs do not allow precise control of thickness and distribution of the guest materials deposited within the pores with depth. This results in uneven pore filling/coating and emitter aggregation within the porous scaffold, which leads to detrimental energy-transfer between emitters and optical scattering/losses and, in turn, to a poor manipulation of the emitter luminescence.

To address these issues, we propose a facile and general strategy called electrostatic nanoassembling for the robust and precise deposition of emitters in nano-mesostructured PSi and, in turn, for the effective PL manipulation of the emitters integrated within PSi-based MCs. To the best of our knowledge, there are no reports on the manipulation of the emission of fluorophores deposited via electrostatic nanoassembling within $PSi/PSiO_2$ MCs.

The electrostatic nanoassembling is a pervasive method for the conformal surface coating of substrates with polymers, colloids, biomolecules, and cells, which offers superior control and versatility with respect to other thin-film deposition methods, especially on micro and nanostructured surfaces.[23] Over the past 20 years, it has been successfully employed for many different applications, from separation science[24] to drug delivery,[25] from biomedicine[26] to biosensing,[27–30] leveraging the electrostatic interaction of oppositely charged nanomaterials (e.g., polyelectrolytes, proteins, nanobeads) and surfaces. The electrically-induced self-regulation of the thickness of single and multilayer films achieved with this approach results in a superior homogeneity and reproducibility of the coating process. This is particularly important for nanostructured materials with high aspect ratio (e.g., nanopores) for which constrained diffusion of molecules and evaporation of solvents might lead to a non-uniform surface coating.[29,31,32]

In this work, we leverage the electrostatic assembling of a nanometer-thick coating of a Rhodamine-labeled cationic polyelectrolyte, namely, poly(allylamine hydrochloride) labeled with Rhodamine B (PAH-RhoB), within the inner surface of a monolithic $PSiO_2$ MC. An enhancing (≈2.5×) and narrowing (≈30×) of the RhoB emission (FWHM = 1.5 nm and Q = 392) at the MC resonance wavelength is achieved, with respect to that of RhoB coated via electrostatic assembling in a non-resonant $PSiO_2$ reference structure. The time-resolved photoluminescence analysis further highlights a shortening (≈20%) of the Rhodamine B emission lifetime within the $PSiO_2$ MC, with respect to that of the reference structure, confirming an increased SE rate through the Purcell effect ($F_p \approx 2.82$) due to a redistribution of the photonic density of state (DOS) of the PAH-RhoB emission in the MC. This is further confirmed by the enhancement of the photoluminescence quantum yield in the $PSiO_2$ MC with respect to the reference structure. Remarkably, the electrostatic nanoassembling of RhoB improves reliability and uniformity of the $PSiO_2$ MC coating process with respect to the direct infiltration of RhoB/PAH blend, thanks to the self-tuned nanometric thickness of the coated PAH-RhoB layer. This minimizes detuning of the cavity optical features strengthening, in turn, modulation of the PAH-RhoB emission with respect to control $PSiO_2$ MCs coated withRhoB/PAH blend (FWHM = 4 nm and Q = 100) using common direct infiltration.

2. Results and Discussion

Preparation and electrostatic coating of $PSiO_2$ MCs with a RhoB-labeled nanometer-thick cationic polyelectrolyte were obtained as sketched in **Figure 1**a. We prepared a monolithic PSi microcavity with thickness of ≈10 µm through an electrochemical etching of crystalline silicon (Figure 1a-i). The microcavity consisted of a low porosity half-wavelength defect sandwiched between two distributed Bragg reflectors (DBRs) made of a series of quarter-wavelength high/low porosity bi-layers. The as-made PSi MC was thermally oxidized to convert silicon to SiO_2 (Figure 1a-ii), so as to achieve a porous silicon oxide microcavity with a hydrophilic, negatively-charged surface. The $PSiO_2$ MC still maintained the integrity of the nanopore framework, enhancing the chemical stability in water-based solutions[28] and reducing the optical absorption losses in the visible region.[6,14]

A red-emitting fluorophore, namely, Rhodamine B (RhoB), was covalently bound to a positively-charged polyelectrolyte, namely, poly(allylamine hydrochloride) (PAH), with a binding ratio 1:145, that is, one molecule of RhoB every 145 monomers of PAH (Figure 1b). The PAH-RhoB polyelectrolyte was solubilized in water and drop cast onto the $PSiO_2$ MC to achieve spontaneous infiltration of the nanopores with the polyelectrolyte solution (Figure 1a-iii). Rinsing in deionized water and ethanol eliminated the excess of polyelectrolyte within the pore volume, leaving a nanometer-thick (i.e., 1.76 ± 0.17 nm, as measured on a SiO_2/Si substrate) monolayer of the positively-charged PAH-RhoB polyelectrolyte anchored to the negatively-charged inner SiO_2 surface of the nanopores by electrostatic forces[33] (Figure 1a-iv).

A $PSiO_2$ layer with constant porosity coated with the same PAH-RhoB polyelectrolyte via electrostatic nanoassembling was then prepared and used as a non-resonant reference structure. Thickness and porosity of such a $PSiO_2$ reference structure were set equal to those (average values) of the $PSiO_2$ MC. Furthermore, a $PSiO_2$ MC coated with a PAH/RhoB blend by direct infiltration was also prepared to investigate the potential advantages of the electrostatic nanoassembling technique with respect to a standard approach.

Figure 1c,e and Figure S1a, Supporting Information, show scanning electron microscopy (SEM) top-view and cross-section images of an as-made PSi MC with 20 high/low porosity

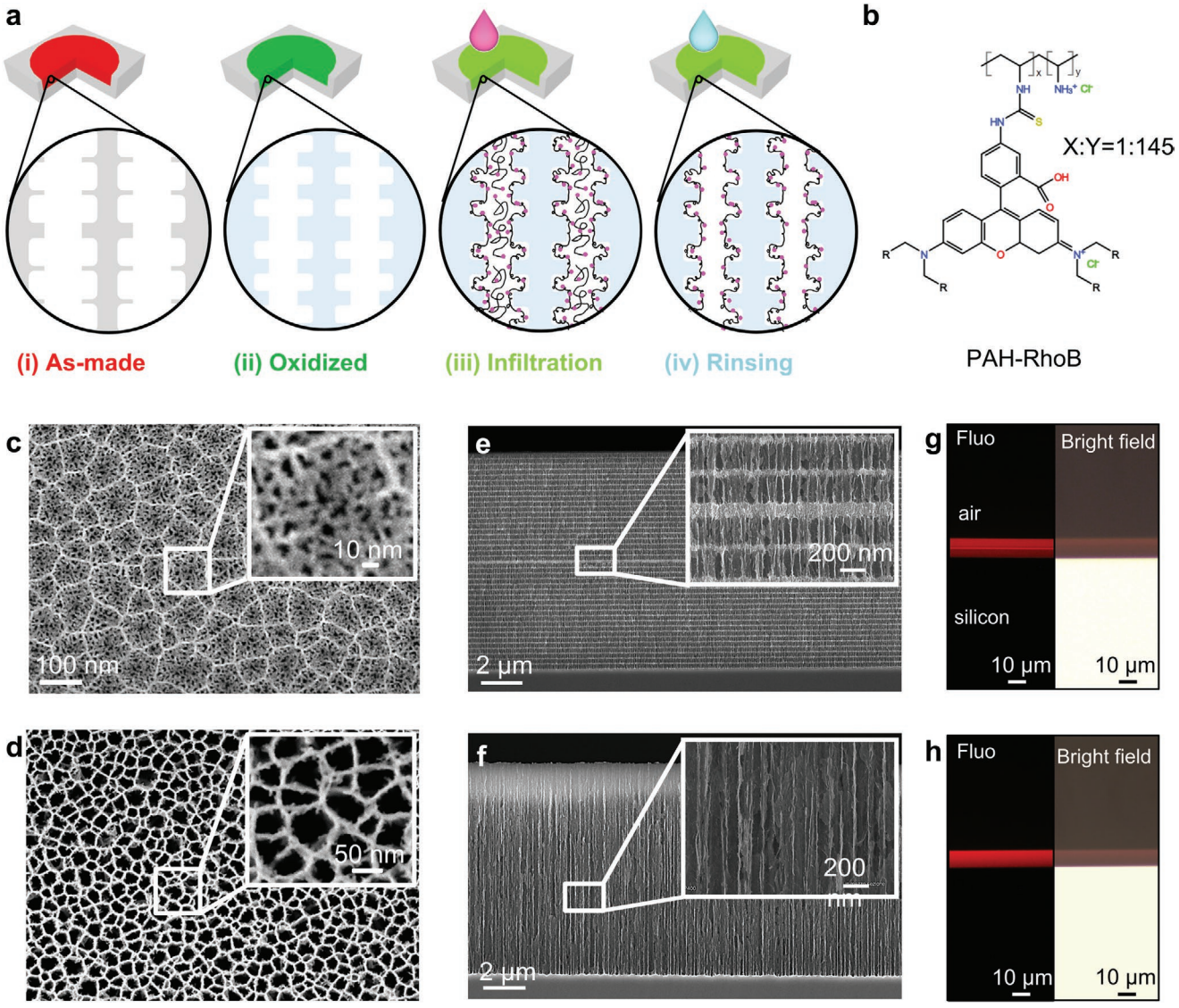

Figure 1. Electrostatic nanoassembling of fluorophores covalently-bound to a cationic polyelectrolyte (PAH-RhoB) within $PSiO_2$ MCs. a) Sketch of the main technological steps for the preparation of the $PSiO_2$ MC coated with PAH-RhoB via electrostatic nanoassembling: i) preparation of a PSi MC via silicon electrochemical etching; ii) thermal oxidation; iii) infiltration of the $PSiO_2$ MC with a positively charged PAH-RhoB solution, and; iv) water and ethanol rinsing to achieve an nm-thick PAH-RhoB coating. b) Chemical structure of the PAH-RhoB light-emitting polyelectrolyte employed for the electrostatic nanoassembling. c,d) Top-view SEM images of the high/low porosity bi-layer of the as-made PSi MC (c) and constant porosity layer of the PSi reference structure (d). Insets show higher magnification images of the PSi structure. e,f) Cross-section SEM images of the as-made PSi MC (e) and reference structure (f). Insets show higher magnification images of the PSi structure. g,h) Fluorescence and bright-field microscope images of the cross-section of the $PSiO_2$ MC (g) and reference (h) structures coated with a monolayer of PAH-RhoB.

quarter-wavelength bi-layers integrated on top and bottom of a (low porosity) half-wavelength defect layer. The square-wave modulation of the porosity and, in turn, of the refractive index of the material along the direction perpendicular to the silicon surface is apparent in Figure 1e, where darker and brighter alternating layers indicate high and low porosity layers, respectively, that is low (≈1.5 refractive index units, RIU at 588 nm) and high (≈2 RIU at 588 nm) refractive index regions. The inset in Figure 1c,e shows a detail of the defect layer of the cavity, also highlighting the different pore morphology and size of high and low porosity layers, namely, straight pores with ≈85 and ≈6 nm diameters, respectively. Size and distribution of the pores in the high and low porosity layers of the PSi MC can be better appreciated from top-view images in Figure S1a, Supporting Information, from which a Gaussian distribution of the pores is achieved, centered at ≈85 and ≈6 nm, respectively (Figure S1c,d, Supporting Information). The morphology, size, and distribution of the pores in the PSi reference structure are shown in Figure 1d,f and Figure S1b,e, Supporting Information, where cylindrical pores with average size of ≈60 nm are visible.

To check the homogeneity of the pore coating with the PAH-RhoB polyelectrolyte over depth, the cross-section of coated $PSiO_2$ MC and reference structures was investigated by fluorescence microscopy. Figure 1g,h shows fluorescence and

bright-field optical microscope images of the cross-section of $PSiO_2$ MC and reference structures coated with the PAH-RhoB polyelectrolyte, respectively. A bright and uniform red emission is observed for both the $PSiO_2$ structures, confirming that the pores are coated with the PAH-RhoB polyelectrolyte over their full depth in spite of their small diameter, which reduces down to 6 nm for the low porosity/high refractive index layer, and high aspect ratio (>100). A local change of the emission intensity in correspondence of defect layer of the cavity is appreciable in Figure 1g for the $PSiO_2$ MC.

To extend our insight into the optical quality of the prepared $PSiO_2$ MC we acquired reflectance spectra at each preparation step (namely, as-made, after oxidation, and after electrostatic coating) (**Figure 2**a). The reflectance spectra of the $PSiO_2$ MC were then compared to those acquired on the non-resonant $PSiO_2$ reference structure (Figure 2b). The as-made PSi MC features a high-reflectance region (99% to 100%) with FWHM (full-width at half maximum) of about 145 nm centered at around 684 nm corresponding to the photonic stopband of the cavity (Figure 2a, black line). The reflectance notch corresponding to the resonance wavelength of the cavity is not resolved for the as-made PSi MC anchored to the native silicon substrate, due to the high refractive index contrast and large absorption coefficient of silicon in the visible range. After thermal oxidation there is a net blue-shift (100 ± 1 nm) of the stopband (FWHM about 84 nm centered at 583 nm), owing to the smaller refractive index of SiO_2 with respect to that of silicon, within which a high reflectance (between 98% and 99%) is still retained (Figure 2a, red line). The cavity mode appears in the middle of the stopband, peaked at 583 nm, thanks to the reduced refractive index contrast of oxidized high and low porosity layers. The Fabry–Pérot interference fringes are now visible below 450 nm, where silicon absorption dominated the reflectance spectrum of the as-made PSi MC. This is a clear indication that most of the silicon in the PSi framework was converted to SiO_2.

Once the PAH-RhoB polyelectrolyte is integrated inside the $PSiO_2$ MC via electrostatic nanoassembling, the resonance wavelength red-shifted by ≈5 ± 1 nm due to the augmented effective refractive index of the $PSiO_2$ structure induced by the guest material. The resonant wavelength is now centered at ≈588 nm and is characterized by a Q factor of 346 (FWHM = 1.7 nm). The stopband still exhibits a reflectivity of 98–99% over a broad spectral range (565–620 nm) (Figure 2a, blue line) enabling a full coverage of the PL spectrum of the PAH-RhoB, peaked at 583 nm with an FWHM of 45 nm (Figure S4a, Supporting Information, red solid line). Furthermore, the lineshape of the reflectance spectrum confirms a uniform coating of the MC with the polyelectrolyte throughout the entire porous nano-/mesostructure, as neither broadening nor additional shoulder are appreciable in the reflectance spectrum.[34] As expected, Fabry–Pérot reflectance fringes dominate the reflectance spectrum of the non-resonant $PSiO_2$ reference structure at any processing step (Figure 2b).

Theoretical reflectance spectra of the as-made, oxidized, and PAH-RhoB coated $PSiO_2$ MC, calculated using the transfer matrix method (TMM),[35] are in good agreement with the

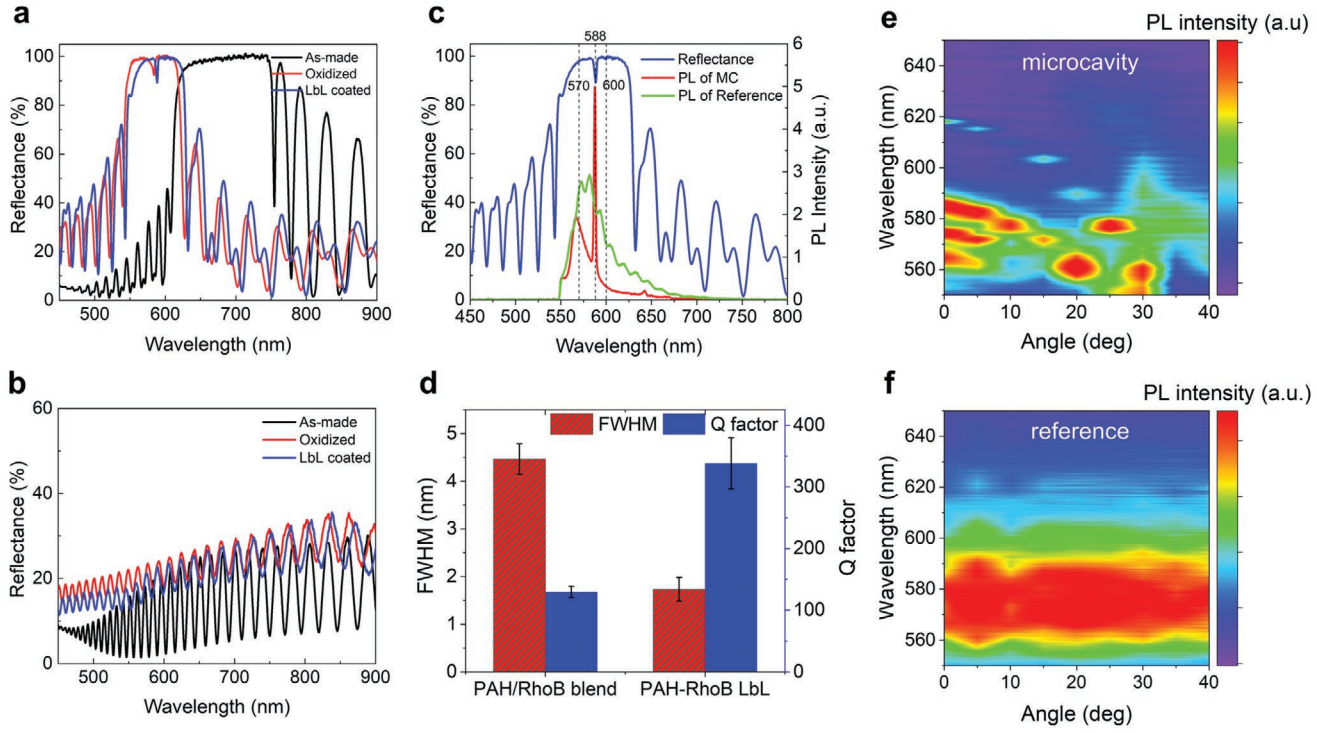

Figure 2. Photoluminescence modulation in $PSiO_2$ MCs coated with PAH-RhoB via electrostatic nanoassembling. a,b) Reflectance spectra of PSi-based MC (a) and reference (b) structures as-made (black lines), oxidized (red lines), and coated with PAH-RhoB (blue lines). c) Reflectance (blue line) and PL spectra of $PSiO_2$ MC (red line) and reference (green line) structures coated with PAH-RhoB. d) FWHM and Q-factor values of the emission of RhoB in $PSiO_2$ MCs coated with PAH-RhoB via electrostatic nanoassembling versus control $PSiO_2$ MCs infiltrated with PAH/RhoB blend. e,f) Angle-resolved PL emission of RhoB in $PSiO_2$ MC (e) and reference (f) structures coated with PAH-RhoB via electrostatic nanoassembling.

experimental spectra at each fabrication step (Figure S2, Supporting Information). Best-fitting of the experimental spectra with theoretical ones provides the amount of residual silicon in the structural skeleton and PAH-RhoB coating on the inner pore walls of the $PSiO_2$ MC, which we estimated to be around 0.4% of the SiO_2 volume and 4% of the air volume, respectively. This value confirms that the nanopores of the PAH-RhoB coated $PSiO_2$ MC are mostly empty (i.e., filled with air), thus corroborating the coating of the inner pore surface with a nanometer thick polymeric layer, in agreement with the literature on electrostatic nanoassembling.[36]

We next investigated the confinement effect of the $PSiO_2$ MC on the PAH-RhoB emission by comparing the PL spectra of PAH-RhoB deposited via electrostatic nanoassembling within the cavity and reference structures. Figure 2c shows the PL spectra of PAH-RhoB coated $PSiO_2$ MC (red line) and reference (green line) structures. To highlight the PL modulation induced by the $PSiO_2$ MC, the emission spectra are superposed to the reflectance spectrum of the cavity (blue line). The PL spectrum of the PAH-RhoB polyelectrolyte is strongly reshaped when integrated in the cavity. The RhoB emission at the resonance wavelength (λ_{peak} = 588 nm) is significantly enhanced (2.5×) and narrowed (30×, FWHM = 1.5 nm and Q = 392) with respect to that of the reference structure, thanks to the effective light confinement within the defect mode of the MC. As expected, the PAH-RhoB deposited in the non-resonant $PSiO_2$ reference structure does not show any significant change of the PL spectrum with respect to that of a PAH-RhoB solution (Figure S4a, Supporting Information).

We also find a small but measurable increase of the PL quantum efficiency of the PAH-RhoB polyelectrolyte in the cavity, with respect to the reference structure, namely, $Q_{MC} \approx 4.5 \pm 0.2\%$ and $Q_{Ref} \approx 4.0 \pm 0.2\%$, respectively.

Infiltration of $PSiO_2$ MCs with a PAH/RhoB blend with same RhoB concentration as the PAH-RhoB solution was also investigated. This allows highigthing the advantages of the electrostatic nanoassembling technique on the manipulation of the RhoB emission with respect to the standard direct infiltration approach. Higher Q factors and smaller FWHM values (≈3×) were achieved for $PSiO_2$ MCs coated with PAH-RhoB by electrostatic nanoassembling, compared to those of cavities infiltrated with the PAH/RhoB blend that are in agreement with typical values reported for PSi-based MCs with direct infiltration of guest emitters (i.e., FWHM > 6 nm and $Q < 100$)[19–22] (Figure 2d and Figure S3, Supporting Information). Infiltration of the PAH/RhoB blend does not allow a fine control of the thickness of the polymer deposited onto the pore surface after solvent evaporation, leading to a spatially-uneven coating of the microcavity with the PAH/RhoB blend, especially when the pore size reduces down to the nanometer range. This strongly affects the line shape of reflectance and emission spectra thereby detuning the resonance and worsening the performance of the cavity, as it is apparent in the reflectance/emission spectra reported in Figure S3d–f, Supporting Information. Conversely, the electrostatic coating with the PAH-RhoB polyelectrolyte results in a conformal nm-thick self-assembled monolayer deposited on the inner surface of the pores,[31,32,37] which minimizes architectural changes thereby keeping resonance and optical quality of the microcavity as designed (Figure S3a–c, Supporting Information). This is also consistent with the improved in-sample and sample-to-sample reliability of the electrostatic nanoassembly process (Figure S3a–c, Supporting Information). A smaller emission intensity (≈3×) of the PAH-RhoB coated $PSiO_2$ MCs is also observed, compared to those coated with the PAH/RhoB blend. This is due to the lower PL quantum yield of the PAH-RhoB (5 ± 0.25%, solution) with respect to that of the PAH/RhoB blend (28 ± 0.49%, solution), with same RhoB concentration (Figure S4a, Supporting Information). The lower emission efficiency of RhoB covalently-bound to PAH can be explained in terms of an inhomogeneous distribution of RhoB within the PAH polymer chain, which results in RhoB quenching due to intermolecular energy-transfer,[38] as also confirmed by pump-probe measurements (Figure S4b,c, Supporting Information). Specifically, whereas in the PAH/RhoB blend solution the stimulated emission signal (580 nm) exhibits an initial fast decay due to vibrational cooling down to the first excited state (1.8 ps) followed by a slow decay (≈2 ns) related to the radiative deactivation to the ground state, the PAH-RhoB solution undergoes an additional deactivation process (8 ps) that is consistent with an intermolecular energy transfer between neighboring RhoB molecules within the PAH polymer chain. The higher Q factor (3×) of the $PSiO_2$ cavity coated with PAH-RhoB partially compensates for the lower emission efficiency of the RhoB covalently-bound to PAH.

The confinement effect of $PSiO_2$ MCs on the emisssion of electrostatically coated PAH-RhoB was also confirmed through angle-resolved measurements (Figure 2e). As the angle increases, the PL emission peak of the RhoB integrated in the cavity shifts to lower wavelengths, consistently with the blue-shift of the resonant mode. As expected, no significant modulation of the emission spectrum is observed when the PAH-RhoB polyelectrolyte is integrated in the $PSiO_2$ reference structure (Figure 2f).

Preparation of PAH-RhoB coated $PSiO_2$ MCs with resonance wavelength detuned (i.e., ≈620 nm) with respect to the emission peak of the RhoB (i.e., ≈580 nm), nicely confirmed the results discussed above for tuned cavities (Figure S5, Supporting Information).

We eventually investigated the excited-state lifetime of PAH-RhoB integrated in the $PSiO_2$ MC and reference structures via electrostatic nanoassembling to get further insight into the radiative and non-radiative decay kinetics.[39] Time-resolved PL measurements were carried out using time-correlated single-photon counting (TCSPC) technique.[39] **Figure 3**a–c shows time-resolved PL intensity profiles of $PSiO_2$ MC and reference structures coated via electrostatic nanoassembling with PAH-RhoB, measured at the resonant wavelength (CM, λ = 588 nm), as well as at the high- and low-energy side stopbands (HSB, λ = 570 nm and LSB, λ = 600 nm). The PL decay at the resonant wavelength (λ = 588 nm) of the $PSiO_2$ MC is significantly shorter than that of the $PSiO_2$ reference. We were able to fit the decay profiles in Figure 3a–c to a bi-exponential function of the form $I(t) = I_1 e^{-t/\tau_1} + I_2 e^{-t/\tau_2}$. Fitting parameters are reported in **Table 1**. The use of a bi-exponential function to fit decay curves of emitting guests in solid hosts is well documented for a number of emitters including, conjugated polymers,[20,40] quantum dots,[41] and also Rhodamine B molecules adsorbed via direct infiltration on porous silica nanoparticles prepared by

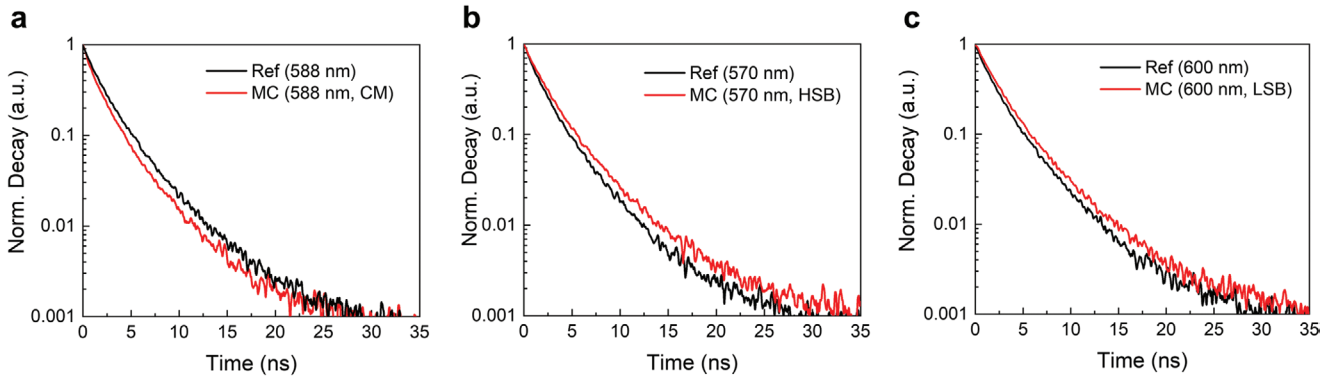

Figure 3. Time-resolved PL intensity of $PSiO_2$ MC and reference structures coated with PAH-RhoB via electrostatic nanoassembling. a,c) Time-resolved PL of a) tuned cavity mode peaked at 588 nm, b) detuned high-energy side stopband mode peaked at 570 nm, and c) detuned low-energy side stopband mode peaked at 600 nm.

chemical synthesis.[42,43] In the latter, the shorter decay time is assigned to the fraction of RhoB molecules that are uniformly dispersed in the pores and have weak interaction with the SiO_2 nanostructure surface; the longer decay time is explained in terms of stronger interaction of RhoB molecules with the SiO_2 nanostructure surface. This is consistent with the electrostatic assembling of RhoB molecules covalently-bound to a PAH polyelectrolyte on the nanostructured $PSiO_2$ surface. Thickness and conformation of polyelectrolytes deposited on a nanostructured surface are indeed mainly dependent on the assembling conditions, for a given polyelectrolyte.[44] Herein, the assembling conditions of the PAH-RhoB polyelectrolyte results in a 1.7-nm-thick folded polyelectrolyte electrostatically bound to the silica surface, in agreement with the literature.[36] Given the labeling degree of RhoB (RhoB:PAH = 1:145, ideally 1 RhoB molecule every 20 nm of PAH), it is reasonable that the folding of the polyelectrolyte deposited on the $PSiO_2$ surface leads to RhoB molecules with different distances from the nanostructured surface.

A significant reduction (≈38% for τ_1 and 19% for τ_2) of both short and long exponential decay times of the PAH-RhoB coated $PSiO_2$ MC was observed at the resonance wavelength $\lambda = 588$ nm, with respect to those of the $PSiO_2$ reference structure (Figure 3a and Table 1), which can be attributed to the enhanced radiative rate of RhoB fluorophores in the cavity with respect to the reference structure (Table S2 and S3, Supporting Information). These findings support the rearrangement of the photonic DOSs inside the cavity at the resonant wavelength, as described by the Fermi's Golden Rule.[22] The redistribution of the DOSs induced by the $PSiO_2$ MC is further corroborated by the observation of longer lifetimes at wavelengths outside the central defect mode (namely, HSB, $\lambda = 570$ nm; and LSB, $\lambda = 600$ nm), compared to those measured on the reference structure (Figure 3b,c and Table 1).

Remarkably, the integration of PAH-RhoB within the $PSiO_2$ MC results in a PL intensity enhancement of a factor ≈2.37 (I_{MC}/I_{Ref}) at the resonance wavelength, with respect to that of the reference structure (Figure 2c). Furthermore, the SE rate in the PAH-RhoB coated $PSiO_2$ MC at the resonance wavelength compared to that in the $PSiO_2$ reference structure is $\tau_{avg\_Ref}/\tau_{avg\_MC} \approx 1.19$ (Table 1). An experimental Purcell factor $F_p \approx 2.82$ is then achieved at the resonance wavelength $\lambda = 588$ nm according to the equation:[45,46]

$$F_p(\lambda) = \frac{I_{MC}(\lambda)}{I_{Ref}(\lambda)} \frac{\tau_{Ref}(\lambda)}{\tau_{MC}(\lambda)} \quad (1)$$

as the product of the ratios of PL intensity enhancement and lifetime reduction between $PSiO_2$ MC and reference structures.

This is in agreement with the observed enhancement of the PL decay rates and radiative and non-radiative rate constants (Table S2 and S3, Supporting Information) in the $PSiO_2$ MC at resonance wavelength, with respect to the non-resonant $PSiO_2$ reference structure, which we assign to the Purcell effect ($F_P > 1$).[47]

To further highlight advantages and flexibility of the proposed approach, we investigated the use of a different polycation (i.e., Polyethyleneimine, PEI) and a different emitter (i.e., Rhodamine 6G, Rho6G) for the coating of $PSiO_2$ MCs via the electrostatic nanoassembling technique (Figure S6, Supporting Information). PL emission of RhoB and Rho6G covalently bound

Table 1. Fitting parameters of time-resolved PL intensity profiles of $PSiO_2$ MC and reference structures coated with PAH-RhoB via electrostatic assembling. PL decay time constants and amplitudes were extracted from best-fitting of the time-resolved PL profiles in Figure 3a–c.

		τ_1 [ns]	τ_2 [ns]	I_1	I_2	$\tau_{avg.}$ [ns]
CM	Microcavity	0.74 ± 0.01	2.57 ± 0.01	0.47 ± 0.01	0.53 ± 0.01	2.20 ± 0.01
	Reference	1.19 ± 0.01	3.17 ± 0.02	0.50 ± 0.01	0.47 ± 0.01	2.61 ± 0.02
HSB	Microcavity	1.36 ± 0.02	3.40 ± 0.03	0.53 ± 0.01	0.45 ± 0.01	2.75 ± 0.03
	Reference	1.06 ± 0.01	2.96 ± 0.02	0.53 ± 0.01	0.47 ± 0.01	2.41 ± 0.02
LSB	Microcavity	1.72 ± 0.02	4.08 ± 0.06	0.70 ± 0.01	0.31 ± 0.01	2.93 ± 0.05
	Reference	1.30 ± 0.01	3.35 ± 0.03	0.56 ± 0.01	0.41 ± 0.01	2.64 ± 0.02

to PEI is strongly reshaped after electrostatic nanoassembling in the $PSiO_2$ cavity (Figure S6g,i, Supporting Information), compared to the broad PL emission of thin films (Figure S6a, Supporting Information), consistently with the results achieved on $PSiO_2$ cavities coated with PAH-RhoB. Similar results were also achieved labeling Rho6G to PAH (Figure 1h).

3. Conclusions

The electrostatic nanoassembling of a positively charged polyelectrolyte engineered with fluorescent molecules (i.e., PAH-RhoB, PEI-RhoB, PAH-Rho6G, PEI-Rho6G) onto the negatively charged inner surface of oxidized $PSiO_2$ MCs was successfully demonstrated as a robust and effective route to manipulate the emission of emitting dyes bound to an nm-thick polymer film. Despite the probable charge-transfer between polyelectrolyte and emitter molecules due to non-uniform Rhodamine distribution along the polymer chain, the electrostatic coating of $PSiO_2$ MCs with PAH-RhoB resulted in an outstanding modulation, in terms of FWHM and Q, of the emission spectrum of the Rhodamine at the resonance mode, as well as in an improved reliability, in terms of thickness and uniformity, of the nanostructure coating with the light-emitting polymer, compared to the standard direct infiltration of a PAH/RhoB blend. The emission of the nanometer-thick monolayer of PAH-RhoB was strongly confined by the size-modulated mesostructured $PSiO_2$ cavity in the out-of-plane direction, with narrow linewidth (down to 1.5 nm), improved PLQY (10% higher than the non-resonant control), fast radiative rate at initial decay process (≈0.74 ns), and sensitive angle-resolved emission (up to 40 degrees). Furthermore, the PAH-RhoB coated $PSiO_2$ MC sustained an experimental Purcell factor F_p of ≈2.82, thus supporting the enhancement of the SE rates of the Rhodamine when incorporated into a resonant cavity via electrostatic nanoassembly coating technology.

Remarkably, the electrostatic nanoassembling technology is a versatile and flexible coating approach that can be applied to diverse polyelectrolytes (both positively and negatively charged), emitters, and materials, with no significant difference in terms of coating performance. In fact, the thickness of electrostatically-assembled coatings is self-tuned to a few nm per layer regardless of the substrate used, which makes the film properties highly controllable and rather independent of the substrate. The polyelectrolyte thickness and conformation on the nanostructured surface and, in turn, the newly created film is indeed mainly dependent on the chosen polyelectrolytes and adsorption conditions, and less dependent on the substrate or the substrate charge density.[44] This makes the approach very general and suitable for different optical materials and platforms.

By building on these results, we envisage many emerging photonic applications of the electrostatic nanoassembly coating technology for introduction of foreign emitters into PSi-based photonic nano-/mesostructures, though not limited to, including ultrasensitive fluorescence-enhanced optical nanosensors, nanolasers, exciton-polaritonic devices, spintronic devices, and quantum optical devices.

4. Experimental Section

Fabrication of PSi MC and Reference Structures: The PSi photonic nano-/mesostructures were prepared by anodic etching of highly doped *p*-type silicon (boron-doped, <100>-oriented, resistivity of 0.8–1.2 mΩ cm, Siltronix, Inc.) with a solution of HF (48%): EtOH (3:1, v/v) at room-temperature. A home-made Teflon cell equipped with two electrodes, namely, an aluminum disk in contact with the silicon substrate as anode and a platinum coil as cathode immersed in the solution, was utilized for the electrochemical-etching over a silicon area of 0.567 cm^2. The etching current density and voltage drop between the silicon sample and the cathode were monitored by using a Keithley 2602A SourceMeter. In detail, a first PSi sacrificial layer was etched at a constant current density of 300 mA cm^{-2} for 10 s, followed by a dissolution step with a solution of NaOH (1 M in DIW):EtOH (9:1, v/v), to avoid formation of a top parasitic layer with pores of a few nanometers in diameter that would restrict diffusion of molecules and polymers underneath. The as-etched silicon samples were thoroughly rinsed with DIW and ethanol before the next electrochemical etching of PSi the photonic nano-/mesostructures. PSi reference structures were etched with a constant current density of 150 mA cm^{-2} for 100 s, with designed thickness of ≈10 µm and porosity of 67%. PSi MCs were etched with a square-wave current density profile of high current density (300 mA cm^{-2}) and low current density (30 mA cm^{-2}) to obtain periodic PSi nano-mesostructured materials consist of high porosity layers (74%; namely, low refractive index, $n_L = 1.5$ at 588 nm) and low porosity layers (59%; namely, high refractive index, $n_H = 2.0$ at 588 nm). The PSi MCs were designed with a half-wavelength defect sandwiched between quarter-wavelength DBRs with 20 (top) and 20 (bottom) high/low porosity bi-layers. The optical thickness of both high and low porosity layers was modulated by tuning the etching time of high and low current density values, so as to ensure that each layer was one quarter of the central mode wavelength of the photonic stop-band of the DBR. The defect layer was etched at 300 or 30 mA cm^{-2} by doubling the etching time of high or low porosity layer of the DBR, so as to obtain an optical thickness of half of the central mode wavelength of the DBR stop-band. The defect layer with low porosity (namely, high refractive index) allowed for better concentration of electromagnetic field inside the microcavity. The entire etching procedure resulted in PSi MCs with a total thickness of ≈10 µm. The PSi samples were cleaned as before described and dried under gentle nitrogen flow. Eventually, the samples were thermally oxidized in a muffle furnace (ZB/1, ASAL) at 750 °C for 3 h with a rump rate of 12 °C min^{-1} in ambient atmosphere to fully convert PSi to $PSiO_2$.

Synthesis of Poly(allylamin hydrochloride) (PAH) and Poly(ethyleneimine) (PEI) with Covalently-Bound Rhodamine B (RhoB) and Rhodamine 6G (Rho6G): 954 mg Poly(allylamine hydrochloride) of molecular weight 40 000 g mol^{-1} was dissolved in 7.5 mL milli-Q water. The pH was set to 8 by means of sodium hydroxide solution. 145 mg of Rhodamine isothiocyanate mixed isomers (Aldrich) dissolved in 4 mL DMF was added to the stirred solution of PAH. The temperature was increased to 50 °C and 4 h incubated under stirring. After cooling down, the pH was decreased to 6 by HCl and the solution dialyzed with a membrane of MWCO 15 000 against milli-Q water for 10 days until Thin Layer Chromatography analysis showed absence of free dye. The solution was freeze-dried and the label degree determined by measuring the absorption intensity of rhodamine at defined polymer concentration (Mol_{Dye}:$Mol_{monomers}$ = 1:145).

For the synthesis of Rho6G labeled polymers, the methyl ester of 1 g Rho6G in 10 mL Ethanol was hydrolyzed by adding 20 mL 2 M NaOH and keeping it boiling under reflux for 12 h. The ethanol was removed by rotation evaporator, the pH set to 6 by HCl. The precipitated free acid of Rho6G was washed with water, and purity was controlled by TLC. 208 mg of the free acid was dissolved in 1.6 mL Dichloroethane and 313 µl POCl3 was added dropwise. After boiling under reflux for 4 h, the solvent was removed by rotation evaporator.

The Rho6G acid chloride was dissolved in 3 mL of tetrahydrofurane and diluted until 0.1 M concentration under UV/Vis control.

100 mg Poly(allylamine hydrochloride) or 50 mg poly(ethyleneimine) was dissolved in 5 mL borate buffer pH 9. 420 µL triethylamine, 1 mL DMF, and 532 µL of the 0.1 M Rho6G acid chloride solution were added, and the mixture was shaken for 1 day at room temperature. The reaction mixture was dialyzed for 2 days (MWCO 15 000 D) against pure water. After freeze-drying the purity was confirmed by TLC and the label degree for PAH-Rho6G determined to 1 dye: 1170 monomer units. For PEI it was determined to1 dye: 1956 monomer units.

Preparation of PAH-RhoB, PEI-RhoB, PAH-Rho6G, PEI-Rho6G (Covalent), PAH/RhoB (Blend) and Pure RhoB Solutions: Solutions of PAH-RhoB, PEI-RhoB, PAH-Rho6G, and PEI-Rho6G (1 mg mL^{-1}, covalent) were prepared in 10 mM acetate buffer + 100 mM NaCl. For control experiments, PAH/RhoB (1 mg mL^{-1} and 0.034 mg mL^{-1}, blend) and pure RhoB (0.034 mg mL^{-1}) solutions with constant PAH/RhoB molar ratio as the PAH-RhoB solution, that is, one molecule of RhoB every 145 monomer of PAH (Mw: ≈40 kDa) were also prepared in acetate buffer.

Electrostatic Nanoassembling of PAH-RhoB, PEI-RhoB, PAH-Rho6G, PEI-Rho6G into $PSiO_2$ Structures: The PAH-RhoB, PEI-RhoB, PAH-Rho6G, PEI-Rho6G solutions (100 µL, 1 mg mL^{-1}) were drop-casted onto the top-surface of oxidized $PSiO_2$ MC and reference structures, and left incubating for 2 h at room temperature to ensure full infiltration of the nanopores with the polymer solution. The samples were then abundantly rinsed with DIW and ethanol for 5 min, and gently dried under a nitrogen flow. For comparison, $PSiO_2$ MCs were also infiltrated with the PAH/RhoB blend solution, following the same procedure.

Materials Characterization: The SEM images were taken using a Zeiss ULTRA55 microscope. The bright-field and fluorescent images of the cross-section of $PSiO_2$ structures coated via electrostatic nanoassembling with PAH-RhoB were captured with a Leica DM2500 M. The thickness of the PAH-RhoB monolayer deposited via electrostatic nanoassembling on a 100-nm-thick SiO_2 layer on top of a Si substrate was measured (3 samples, 3 points per each sample) by ellipsometry (Rudolph Ellipsometer AutoEL II).

Numerical Calculations: The TMM was employed for simulation and calculation of theoretical reflectance spectra of PSi-based MCs, using a home-made Matlab program. The effective refractive indexes of the PSi-based materials were estimated using Bruggemann's equation, iteratively solved with the Newton method.[48] The experimental spectra were best fitted with the theoretical ones within the wavelength window 400 to 900 nm.

Optical Characterizations: Absorption and reflectance spectra were recorded with an Ocean Optics spectrometer (HR4000) equipped with a fiber-coupled Ocean Optics DH-2000 deuterium-halogen lamp. Steady-state PL spectra were acquired by excitation at 520 nm with a continuous-wave (C.W.) laser (Thorlabs) and collection of the PL spectra (also angle-resolved) with an Ocean Optics spectrometer (HR4000). PLQY measurements were carried out by a home-made integrating sphere system in combination with a C.W. laser at 560 nm (Oxxius) and an Ocean Optics spectrometer (Ocean Optics Maya Pro 2000). Time-resolved PL measurements were carried out in air and at room temperature with a TCSPC spectrometer (LifeSpec II, Edinburgh Instruments). Samples were excited at 445 nm with a picosecond pulsed diode laser (EPL 445). Ultrafast TA spectra were conducted by using a home-built ultrafast fs pump-probe system.[49] Briefly, pump wavelength (560 nm, repetition rate 250 kHz) was generated by using a commercial optical parametric amplifier (OPA, Coherent 9450). The OPA was provided with 50 fs pulses at 800 nm wavelength generated by a mode-locked Ti:sapphire oscillator (Coherent Micra) in conjunction with a regenerative amplifier (Coherent RegA 900). The pump laser beam was focused with a 150 mm lens before the sample. As a probe pulse, we used a broadband white light supercontinuum generated in sapphire plate in the spectral region from 450 to 750 nm.

Supporting Information

Supporting Information is available from the Wiley Online Library or from the author.

Acknowledgements

Z.C. and V.R. contributed equally to this work. The authors acknowledge Stefanie Neutzner for helping with pump-probe measurements and Martina Corsi for helping with ellipsometry measurements. G.B. and Z.C. acknowledges the European Community and the Tuscany Region for their funding within the framework of the SAFE WATER project (European Union's Horizon 2020 Research & Innovation program and the ERA-NET "PhotonicSensing" cofund – G.A. No 688735). G.M.P. thanks Fondazione Cariplo by (grant n° 2018-0979) for financial support. F.C. and A.M. acknowledge funding by EPSRC (grant EP/P006280/1, MARVEL), and G.C. and V.R. the European Community's H2020 ETN MSCA action under grant agreement 643238 (SYNCHRONICS). F.C. acknowledges the Royal Society and the Wolfson Foundation for a Royal Society Wolfson Foundation Research Merit Award.

Conflict of Interest

The authors declare no conflict of interest.

Data Availability Statement

Research data are not shared.

Keywords

electrostatic nanoassembly coating, functionalized fluorophores, nanoscale photoluminescence, photonic manipulation, porous silicon oxide microcavities

Received: January 7, 2021
Revised: June 3, 2021
Published online: August 2, 2021

[1] L. T. Canham, *Appl. Phys. Lett.* **1990**, *57*, 1046.
[2] A. G. Cullis, L. T. Canham, *Nat. Mater.* **1991**, *353*, 335.
[3] C. R. Ocier, C. A. Richards, D. A. Bacon-Brown, Q. Ding, R. Kumar, T. J. Garcia, J. van de Groep, J.-H. Song, A. J. Cyphersmith, A. Rhode, A. N. Perry, A. J. Littlefield, J. Zhu, D. Xie, H. Gao, J. F. Messinger, M. L. Brongersma, K. C. Toussaint, L. L. Goddard, P. V. Braun, *Light: Sci. Appl.* **2020**, *9*, 196.
[4] N. A. Krueger, A. L. Holsteen, S. K. Kang, C. R. Ocier, W. Zhou, G. Mensing, J. A. Rogers, M. L. Brongersma, P. V. Braun, *Nano Lett.* **2016**, *16*, 7402.
[5] Y. Wan, N. A. Krueger, C. R. Ocier, P. Su, P. V. Braun, B. T. Cunningham, *Adv. Opt. Mater.* **2017**, *5*, 1700605.
[6] C. R. Ocier, N. A. Krueger, W. Zhou, P. V. Braun, *ACS Photonics* **2017**, *4*, 909.
[7] H. Ning, N. A. Krueger, X. Sheng, H. Keum, C. Zhang, K. D. Choquette, X. Li, S. Kim, J. A. Rogers, P. V. Braun, *ACS Photonics* **2014**, *1*, 1144.
[8] M. J. Sailor, E. C. Wu, *Adv. Funct. Mater.* **2009**, *19*, 3195.
[9] M. J. Sailor, *Porous Silicon in Practice: Preparation Characterization and Applications*, Wiley-VCH, Weinheim, Germany, **2012**.
[10] V. S.-Y. Lin, K. Motesharei, K.-P. S. Dancil, M. J. Sailor, M. R. Ghadiri, *Science* **1997**, *278*, 840.
[11] S. Mariani, V. Robbiano, R. Iglio, A. A. La Mattina, P. Nadimi, J. Wang, B. Kim, T. Kumeria, M. J. Sailor, G. Barillaro, *Adv. Funct. Mater.* **2019**, *30*, 1906836.
[12] D. S. Barth, C. Gladden, A. Salandrino, K. O'Brien, Z. Ye, M. Mrejen, Y. Wang, X. Zhang, *Adv. Mater.* **2015**, *27*, 6131.

[13] S. Demchyshyn, J. M. Roemer, H. Groiß, H. Heilbrunner, C. Ulbricht, D. Apaydin, A. Böhm, U. Rütt, F. Bertram, G. Hesser, M. C. Scharber, N. S. Sariciftci, B. Nickel, S. Bauer, E. D. Głowacki, M. Kaltenbrunner, *Sci. Adv.* **2017**, *3*, e1700738.
[14] N. Massad-Ivanir, S. K. Bhunia, N. Raz, E. Segal, R. Jelinek, *NPG Asia Mater* **2018**, *10*, e463.
[15] V. K. Dwivedi, K. Pradeesh, G. Vijaya Prakash, *Appl. Surf. Sci.* **2011**, *257*, 3468.
[16] S. N. Jenie, S. Pace, B. Sciacca, R. D. Brooks, S. E. Plush, N. H. Voelcker, *ACS Appl. Mater. Interfaces* **2014**, *6*, 12012.
[17] S. N. A. Jenie, S. E. Plush, N. H. Voelcker, *Langmuir* **2017**, *33*, 8606.
[18] H. Qiao, B. Guan, T. Böcking, M. Gal, J. J. Gooding, P. J. Reece, *Appl. Phys. Lett.* **2010**, *96*, 161106.
[19] F. S. H. Krismastuti, S. Pace, N. H. Voelcker, *Adv. Funct. Mater.* **2014**, *24*, 3639.
[20] V. Robbiano, S. Surdo, A. Minotto, G. Canazza, G. M. Lazzerini, S. M. Mian, D. Comoretto, G. Barillaro, F. Cacialli, *Nanomater. Nanotechnol.* **2018**, *8*, 184798041878840.
[21] D. Dovzhenko, I. Martynov, P. Samokhvalov, E. Osipov, M. Lednev, A. Chistyakov, A. Karaulov, I. Nabiev, *Opt. Express* **2020**, *28*, 22705.
[22] V. Robbiano, G. M. Paterno, A. A. La Mattina, S. G. Motti, G. Lanzani, F. Scotognella, G. Barillaro, *ACS Nano* **2018**, *12*, 4536.
[23] C. S. Peyratout, L. Dahne, *Angew. Chem., Int. Ed.* **2004**, *43*, 3762.
[24] N. Joseph, P. Ahmadiannamini, R. Hoogenboom, I. F. J. Vankelecom, *Polym. Chem.* **2014**, *5*, 1817.
[25] S. De Koker, R. Hoogenboom, B. G. De Geest, *Chem. Soc. Rev.* **2012**, *41*, 2867.
[26] Z. Poon, D. Chang, X. Zhao, P. T. Hammond, *ACS Nano* **2011**, *5*, 4284.
[27] M. Olszyna, A. Debrassi, C. Üzüm, L. Dähne, *Adv. Funct. Mater.* **2019**, *29*, 1805998.
[28] S. Mariani, A. Paghi, A. A. La Mattina, A. Debrassi, L. Dahne, G. Barillaro, *ACS Appl. Mater. Interfaces* **2019**, *11*, 43731.
[29] S. Mariani, V. Robbiano, L. M. Strambini, A. Debrassi, G. Egri, L. Dahne, G. Barillaro, *Nat. Commun.* **2018**, *9*, 5256.
[30] J. Zhang, J. Zhong, Y. F. Fang, J. Wang, G. S. Huang, X. G. Cui, Y. F. Mei, *Nanoscale* **2014**, *6*, 13646.
[31] J. J. Richardson, J. Cui, M. Bjornmalm, J. A. Braunger, H. Ejima, F. Caruso, *Chem. Rev.* **2016**, *116*, 14828.
[32] G. Decher, *Science* **1997**, *277*, 1232.
[33] P. Bieker, M. Schönhoff, *Macromolecules* **2010**, *43*, 5052.
[34] J. Wang, G. Y. Lee, R. Kennard, G. Barillaro, R. H. Bisiewicz, N. A. Cortez Lemus, X. C. Cao, E. J. Anglin, J. S. Park, A. Potocny, D. Bernhard, J. Li, M. J. Sailor, *Chem. Mater.* **2017**, *29*, 1263.
[35] M. Born, E. Wolf, *Principles of Optics: Electromagnetic Theory of Propagation, Interference and Diffraction of Light*, Elsevier, Cambridge, UK **2013**.
[36] Y. Wang, A. Yu, F. Caruso, *Angew. Chem., Int. Ed.* **2005**, *44*, 2888.
[37] G. Decher, J. B. Schlenoff, *Multilayer Thin Films: Sequential Assembly of Nanocomposite Materials*, Wiley-VCH, Weinheim, Germany **2006**.
[38] J. Kang, O. Kaczmarek, J. Liebscher, L. Dähne, *Int. J. Polym. Sci.* **2010**, *2010*, 264781.
[39] C. E. Rowland, I. Fedin, H. Zhang, S. K. Gray, A. O. Govorov, D. V. Talapin, R. D. Schaller, *Nat. Mater.* **2015**, *14*, 484.
[40] J. Cornil, D. Beljonne, J. P. Calbert, J. L. Brédas, *Adv. Mater.* **2001**, *13*, 1053.
[41] A. F. van Driel, I. S. Nikolaev, P. Vergeer, P. Lodahl, D. Vanmaekelbergh, W. L. Vos, *Phys. Rev. B* **2007**, *75*, 035329.
[42] B. Martins Estevão, I. Miletto, L. Marchese, E. Gianotti, *Phys. Chem. Chem. Phys.* **2016**, *18*, 9042.
[43] H.-H. Rao, Z.-H. Xue, G.-H. Zhao, S.-Y. Li, X. Du, *J. Non-Cryst. Solids* **2016**, *450*, 32.
[44] S. T. Dubas, J. B. Schlenoff, *Macromolecules* **2001**, *34*, 3736.
[45] J. E. Fröch, S. Kim, C. Stewart, X. Xu, Z. Du, M. Lockrey, M. Toth, I. Aharonovich, *Nano Lett.* **2020**, *20*, 2784.
[46] D. Englund, B. Shields, K. Rivoire, F. Hatami, J. Vučković, H. Park, M. D. Lukin, *Nano Lett.* **2010**, *10*, 3922.
[47] S. Noda, M. Fujita, T. Asano, *Nat. Photonics* **2007**, *1*, 449.
[48] A. M. Ruminski, G. Barillaro, C. Chaffin, M. J. Sailor, *Adv. Funct. Mater.* **2011**, *21*, 1511.
[49] G. M. Paternò, L. Moretti, A. J. Barker, Q. Chen, K. Müllen, A. Narita, G. Cerullo, F. Scotognella, G. Lanzani, *Adv. Funct. Mater.* **2019**, *29*, 1805249.